IEEE Access
Multidisciplinary : Rapid Review : Open Access Journal

Received August 13, 2020, accepted September 27, 2020, date of publication October 7, 2020, date of current version October 22, 2020.

Digital Object Identifier 10.1109/ACCESS.2020.3029355

Reference-Free Material Characterisation of Objects Based on Terahertz Ellipsometry

BENEDIKT FRIEDERICH, DILYAN DAMYANOV, JAN C. BALZER, AND THORSTEN SCHULTZE
Chair of Communication Systems, University of Duisburg-Essen, 47057 Duisburg, Germany
Corresponding author: Dilyan Damyanov (dilyan.damyanov@uni-due.de)

This work was supported by the Deutsche Forschungsgemeinschaft (DFG, German Research Foundation) Project-ID 287022738 TRR 196, Project M05. We acknowledge support by the Open Access Publication Fund of the University of Duisburg-Essen.

ABSTRACT Material characterization in the 0.1 – 10 THz range has been a major topic of research since its first demonstration 30 years ago. Advances in terahertz generation, detection, and data acquisition have contributed to improved bandwidth, signal power and signal-to-noise ratio. However, material characterization is still performed using conventional spectroscopic measurement schemes which require detailed information about the test object's shape, location, orientation relative to the measurement system, and a reference measurement. Here, we present a method for reference-free material characterization of dielectric objects using a terahertz time-domain spectroscopy system without *a priori* knowledge about the object and its position. The proposed method is based on ellipsometry combined with lensless imaging for the estimation of the refractive index. The method is a multistage procedure designed for small test objects in reflection mode. The diffracted terahertz radiation is separated from the specular reflected radiation in a post-processing step to enable a valid material parameter estimation. In this way, small dielectric objects can be located, imaged with a sub-mm resolution, and their material parameters extracted.

INDEX TERMS Material characterization, refractive index, THz imaging.

I. INTRODUCTION

Terahertz time-domain spectroscopy (THz TDS) is since the first laboratory demonstration in 1989 [1] an important tool for scientific and industrial applications [2]. The unique feature of THz radiation is the ability to penetrate optically opaque dielectric and nonpolar materials. This enables the detection and imaging of subsurface objects. In comparison to microwaves, the frequency is much higher and hence the maximum obtainable image resolution is better for THz systems. Further, the frequency bandwidth is much higher. Typical THz TDS systems achieve a bandwidth of more than 6 THz [3], [4], which makes these systems interesting for spectroscopic applications. In comparison to X-rays, THz radiation is nonionizing and thus harmless. THz TDS is especially sensitive in transmission mode configuration. By applying sophisticated algorithms for material parameter extraction [5], [6] slightest changes of the refractive index of materials and liquids can be sensed [7]. The general principle of the material parameter extraction is the calculation of the transfer function of the material. This is achieved by dividing a measurement with the empty transmission channel through a measurement with the material under test. For a collimated beam, the exact position of the sample is noncritical. Only the incident angle is important [8]. However, in many real live scenarios and spectroscopy on highly absorbing materials, transmission mode spectroscopy is not feasible. First reflection measurements in the THz frequency range were performed on water [9]. Water has a very high absorption coefficient and can hence only be measured as a very thin film (<100 μm). This may lead to inaccuracy of the determined parameters. In a reflection measurement, the radiation does not need to penetrate the complete sample. The Fresnel equations can be used to calculate the absorption coefficient α and the refractive index n, if the interface between the sample and the surrounding medium (usually air) is well-defined [10]. Nevertheless, it is still necessary to eliminate the influence of the transmission channel (THz path) on the measurement. Therefore, a reference measurement must be performed, where a highly reflective reference is placed at the exact position of the sample. Some efforts have been made to minimize the influence of a slight difference between sample and reference position [11], [12]. Further, it has been demonstrated that also the diffuse reflection can be used to get spectroscopic information from a sample [13], [14]. Here, the Kramers-Kronig transform was used to retrieve the complex refractive

The associate editor coordinating the review of this manuscript and approving it for publication was Pia Addabbo.

index without regarding the phase of the measurement. This is an important step towards a realistic application scenario, where often only measurements in reflection mode are feasible. However, the accuracy is restricted due to the limited frequency response. A promising reference-free approach for the extraction of material parameters is THz ellipsometry. For a known angle of incidence and two orthogonal polarization states, the material parameters can be calculated from the Fresnel equations. However, the position and the shape of the object must be known *a priori*. Further, diffraction from edges and corners reduces the validity of this approach. This limits the field of application to well-defined laboratory experiments.

To overcome this limitations, we present a novel approach for robust and direct measurement of the material parameters in reflection mode by employing THz ellipsometry without *a priori* information about the shape and position of the object under test. The approach is based on a lenseless sensing technique based on parallel (p) and perpendicular (s) polarized THz waves and can be divided into four major steps. First, an image of the sample is reconstructed using migration imaging technique for THz TDS systems [15]. In the next step, the shape of the sample is extracted from the migrated image by employing an active contour extraction method. Next, the features of the object such as corners and edges are detected. Finally, by combining the information from the s and p polarized waves with the information of the shape and position of the sample the characterization of dielectric materials is performed based on THz ellipsometry [18]. By using this approach, we can extract a complete description of the sample's characteristics such as shape, position, and material parameters. To demonstrate the capabilities of the presented approach, two objects constructed from dielectric materials with different size and shape are characterized. A state-of-the-art THz TDS system is used in reflection mode for the measurement scenario.

II. TERAHERTZ ELLIPSOMETRY

Ellipsometry is a well established reference-free reflection-mode characterization technique for the evaluation of material parameters in the optical range [17]. Recently, it has been applied to the microwave range and has proven high accuracy [18]–[22]. The basic principle of ellipsometry is based on the comparison of the difference between the reflection of the p and the s polarization. It utilizes the material dependent differences in the reflection coefficients for a known angle of incidence. An ellipsometric setup can be realized for a linear polarized emitter and detector if s- and p-components are equal in amplitude [18], [19]. In Fig. 1, the experimental setup for ellipsometric measurements is depicted. Here, the emitter **E** and the detector **D** are positioned such that the s- and p-polarized electric fields are generated and transmitted onto the sample surface at an angle $\theta_\mathrm{i} = 45°$ to the plane of incidence. E_i represents the incident terahertz electric field at the material surface and E_r is the specular reflection. For a non-magnetic material, i.e. materials with a permeability

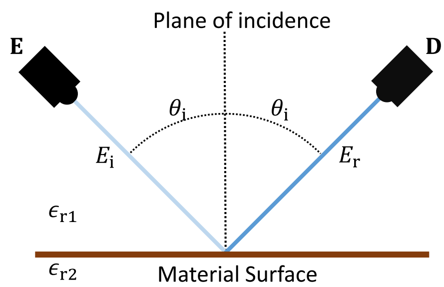

FIGURE 1. **Experimental setup for ellipsometric measurements. The incidence wave E_i (shown light blue) radiated from the emitter E is reflected from an infinite large flat surface as the specular reflected wave E_r (in dark blue) at the detector D.**

of $\mu_\mathrm{r} \approx 1$, the specular reflection is $E_\mathrm{r} = rE_\mathrm{i}$, where r is the material specific reflection coefficient. Considering dielectric materials, the reflection coefficients for s and p differ and are dependent on the complex relative permittivity of the medium in which the wave propagates $\epsilon_{\mathrm{r}1}$ and the material under test $\epsilon_{\mathrm{r}2}$. Hence, the reflected waves from dielectric materials for the two polarizations are $E_{\mathrm{r,s}} = r_\mathrm{s}E_\mathrm{i}$, where r_s is the reflection coefficient for perpendicular polarization, and $E_{\mathrm{r,p}} = r_\mathrm{p}E_\mathrm{i}$, where r_p is the reflection coefficient for parallel polarization. The complex ratio of the reflected perpendicular and parallel electric fields $E_{\mathrm{r,s}}$ and $E_{\mathrm{r,p}}$, respectively, is defined as ρ, and expressed by

$$\rho = \frac{E_{\mathrm{r,p}}}{E_{\mathrm{r,s}}} = \frac{r_\mathrm{p}}{r_\mathrm{s}}. \tag{1}$$

The estimation of the refractive index n is performed by the inverse application of the Fresnel equations [18]. For smooth or slightly rough surfaces in air ($\epsilon_{r,1} \approx 1$) the refractive index is estimated by

$$n_{\mathrm{r},2} = n_\mathrm{r} = \sqrt{\left(\frac{\sin^2(\theta_\mathrm{i})\left(\frac{E_\mathrm{s}}{E_\mathrm{p}} - 1\right)}{\cos(\theta_\mathrm{i})\left(\frac{E_\mathrm{s}}{E_\mathrm{p}} + 1\right)}\right)^2 + \sin^2(\theta_\mathrm{i})} \tag{2}$$

with the angle of incidence θ_i.

This technique provides a good solution for objects with large flat surfaces, where only the specular reflection is considered. For thin-film or multi-layer structures, the estimation must be performed for each frequency point individually. Furthermore, for complex object with edges and corners, not only the specular reflection but also the diffracted electric field from the edges and corners of the objects have to be considered. Hence, the diffraction model for complex objects is considered in the following sub-section.

A. DIFFRACTION OF COMPLEX OBJECTS

The reflection of an object's surface depends not only on the material properties such as the permittivity, but also on the object's shape i.e. edges or corners. At these discontinuities, the electric field is diffracted and may interfere with the specular reflection. As the evaluation of the material parameters using ellipsometry is based on the ratio of two orthogonal

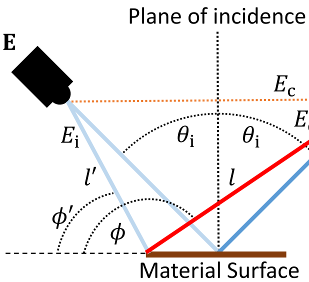

FIGURE 2. Schematic representation of specular (E_r) and diffuse (E_d) reflections from a test object's surface, and the propagating electric field E_c from emitter (E) to detector (D).

polarization states of the specular reflection, the interference with the diffuse reflection leads to errors.

Fig. 2 shows the diffuse (E_d) and specular (E_r) reflection from an incident electric field (E_i) at the surface of an object as well as the cross-talk (E_c) between the emitter and detector. The corresponding electric field E at the detector is a function of the superposition of E_r, E_d and E_c and is determined as

$$E = E_r + E_d + E_c. \tag{3}$$

In order to ensure the suitability of a measurement for material characterization, it is necessary to determine the scattering of the object's edges and E_c, which is considered in the following sub-section. In [26] Luebbers introduces an approximation for the polarization dependent diffraction coefficient $D_{p,s}$ for the calculation of the diffracted electric field by the geometrical theory of diffraction. The geometrical theory of diffraction is an extension of the geometrical optics, which allows to describe the interference at the detector between diffracted rays, specular reflected rays and directly received rays. Important scattering parameters as polarization, conductivity, refractive index, and surface roughness are considered for the calculation of $D_{p,s}$. Using the diffraction coefficient, the diffracted electric field at the point of the detector can be calculated by [23]:

$$E_d = E_{r,p/s} \frac{e^{-jkl'}}{l'} D_{p/s} \cdot \sqrt{\frac{l'}{l(l'+l)}} e^{-jkl}, \tag{4}$$

with k the angular wavenumber, the angles ϕ and ϕ', and the path length l and l'. Thus, if one of the parameters of E_d is incorrectly estimated, the diffracted electric field cannot be correctly compensated in (3) and will lead to an error in the estimated material parameters. To overcome this issue, we propose a method for the detection of the specular reflection from objects for the estimation of the material parameters.

B. EXPERIMENTAL SETUP AND CALIBRATION ROUTINE

The measurements presented in this work are carried out with the THz TDS system TERA K15, from Menlo Systems. Fig. 3 shows a schematic diagram of the experimental setup. It consists of the femtosecond laser source C-Fiber 780, a high-resolution computer-controlled 1600 ps long optomechanical delay unit (ODU), a fiber-coupled terahertz emitter (TERA 15-TX-FC Fe:InGaAs) and a fiber-coupled terahertz detector (TERA 15-RX-FC LT InGaAs). The antennas are mounted in reflection geometry with $\theta = 45°$ for the purpose of ellipsometric measurements (cf. Fig. 1 and Fig. 3). The antennas are separated by 0.26 m and the distance to the center of the rotation stage is 0.13 m.

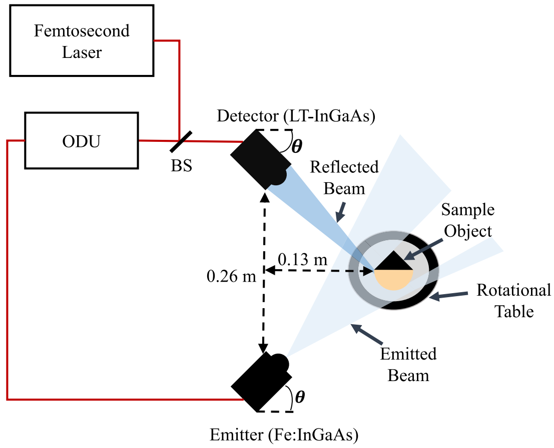

FIGURE 3. Schematic drawing of the experimental setup. The emitter and detector antennas are rotated with $\theta = 45°$ angle to each other. The object under test is mounted on a rotation unit and rotated 360° degree-wise.

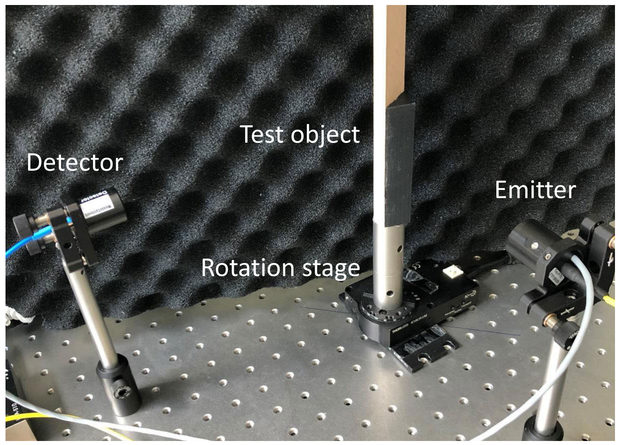

FIGURE 4. Photograph of the measurement setup.

As shown in Fig. 3, a test object is positioned on the rotation stage allowing for a 360° 2-dimensional circular scan. The test object is rotated with an angular resolution of 1° so that 360 measurements can be recorded for the material characterization. A photograph of the measurement setup is shown in in Fig. 4. Here, the detector, the emitter, the test object, and the rotation stage are shown. As demonstrated in the figure, no mirrors or lenses are used to collimate or focus the terahertz beam. For the material parameter estimation, polarimetric measurements are required so that 360° measurements are performed with parallel and perpendicular polarization. However, before the measurements of the test objects are performed, a calibration of the system is required to compensate the antennas and channel characteristics for the precise estimation of the material parameters.

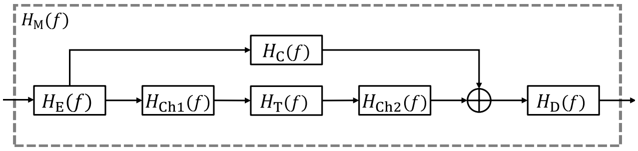

FIGURE 5. **Block diagram of the underlying channel model $H_M(f)$ represented by the system functions of the emitter ($H_E(f)$), and detector antennas ($H_D(f)$), the sample ($H_T(f)$), the direct channel between emitter and detector antennas ($H_C(f)$), the channel from the emitter to the sample ($H_{Ch1}(f)$), and the channel from the sample to the detector ($H_{Ch2}(f)$), respectively.**

In Fig. 5, the channel model for the measurement system is introduced. The system function of the measurement system $H_M(f)$ can be described as

$$H_M(f) = H_E(f) \cdot H_{Ch1}(f) \cdot H_T(f) \cdot H_{Ch2}(f) \cdot H_D(f) + H_E(f) \cdot H_C(f) \cdot H_D(f), \quad (5)$$

where $H_E(f)$ is the system functions of the emitter, $H_D(f)$ is the system function of the detector, $H_T(f)$ is the system function of the test object, $H_C(f)$ is the system function of the direct channel between emitter and detector, $H_{Ch1}(f)$ is the system function of the channel from the emitter to the sample, and $H_{Ch2}(f)$ is the system function of the channel from the sample to the detector. For slowly varying system functions of the channels, the following is employed [15].

At first, an empty measurement $H_{Empty}(f)$ is performed where no test object is in front of the antennas so that the object's system function must be $H_T(f) = 0$. The system function of this calibration measurement is then

$$H_{Empty}(f) = H_E(f) \cdot H_C(f) \cdot H_D(f) \quad (6)$$

In a second step, a reference measurement $H_R(f)$ with an ideal reflector is recorded. As an ideal reflector, a metal plate is used so that the object's system function is

$$H_R(f) = H_E(f) \cdot H_{Ch1}(f) \cdot H_{Ch2}(f) \cdot H_D(f) + H_E(f) \cdot H_C(f) \cdot H_D(f). \quad (7)$$

By using the equations (5) to (7), the object's transfer function is extracted and is determined as

$$H_T(f) = \frac{H_M(f) - H_{Empty}(f)}{H_R(f) - H_{Empty}(f)}. \quad (8)$$

The calibration is performed for s and p polarization and is used for the further processing of the proposed object characterization algorithm.

III. ELLIPSOMETRIC MATERIAL PARAMETER ESTIMATION OF COMPLEX SHAPED OBJECTS

The employed method for the estimation of the material parameters is based on the Fresnel equations from section II. However, to precisely estimate the material parameters, the exact position and orientation of the object relative to the emitter and detector must be known. Furthermore, as only the specular reflections from the test objects will be considered for the calculations, they must be correctly detected. Hence, the shape of the object must be known.

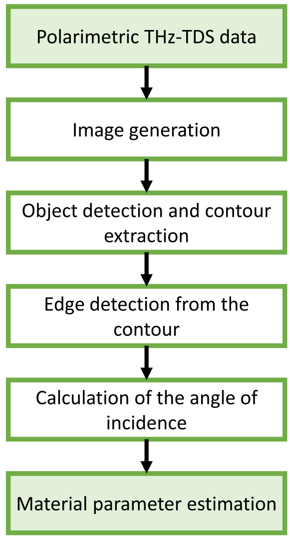

FIGURE 6. **The flowchart of the proposed reference-free material characterisation of objects based on terahertz ellipsometry.**

Thus, we propose an approach for the estimation of the material parameters using THz waves in four steps where in each step a new feature of the object under test is determined. A flowchart depicting the proposed approach is presented in Fig. 6. First, an image of the object is reconstructed followed by the extraction of the shape of the object. Next, the contour features such as corners and edges are detected. Finally, the refractive index of the dielectric object is calculated using the Fresnel equations and the corrected angle of incidence. In the following sub-sections, each step of the proposed approach is described and analyzed for two test objects.

A. KIRCHHOFF MIGRATION BASED IMAGING

Typical imaging setups for the terahertz frequency range employ lenses and/or mirrors to focus the terahertz beam on the surface of a test object at a known distance and orientation [27]–[29]. These imaging setups provide a high lateral resolution if a good optical alignment is achieved. However, even under ideal conditions focusing is achieved only for a very limited focal depth and the terahertz imaging resolution is hindered by the frequency-dependent spot size. Finally, *a priori* information about the distance and orientation of the sample is required for correct imaging. This makes the focused approach unsuitable for applications where no *a priori* information is available or subsurfaces of different orientation are of interest.

Another approach is based on a divergent terahertz beam and the focusing of the image by digital post-processing, typically referred to as migration-based imaging [15], [30]. This approach makes use of the complete frequency bandwidth of the system and allows for image resolution in the sub-mm range. These algorithms rely on the migration-based radar image reconstruction technique first presented by Schneider in [32]. Since then, this technique has been successfully implemented for different radar applications scenarios [33], [34]. For the generation of the images, we employ the

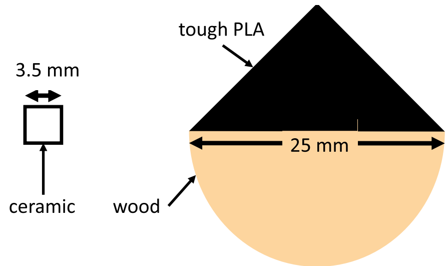

FIGURE 7. Sketch of the two test objects used for the evaluation of the proposed approach. The first test object is a ceramic square post with an edge length of 3.5 mm (shown left) and the second object (shown on the right) is a composite object build from wood (shown in the figure as the brown half-circle) and tough PLA (shown as the black triangle).

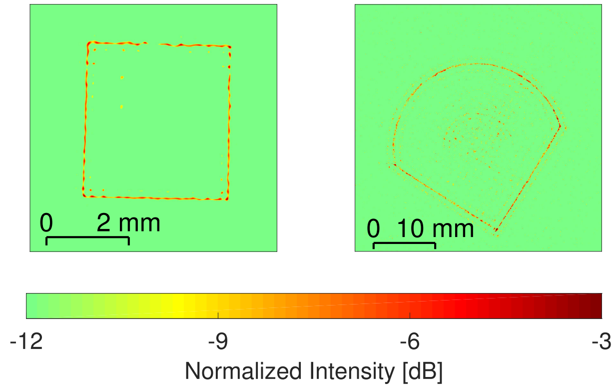

FIGURE 8. Generated image of the two test objects (left ceramic square post and right composite object) using the THz measurements with a s polarization.

Kirchhoff migration imaging method for lensless terahertz measurements as presented in [15].

The Kirchhoff migration produces in the case of bistatic antennas and a 2D object an overlay of 2D images. Here for each reflection at an object shown in the radargram a 2D elliptical wavefront according to the specific round-trip-time is emerging at the emitter and thus this elliptical wavefront is overlayed and becomes a part of the final image. Initially, each pixel in the matrix is set to zero. Afterwards, the amplitudes of the measured scalar field at each antenna position are mapped onto the matrix. Finally, the produced image is a pixel matrix where each element is the result of the superposition of all the received reflections at each antenna position. As a result, the image is focused due to the constructive and destructive interference of the electric fields measured in the individual scans with the synthetic antenna aperture.

For the introduction of the proposed method, we have chosen two exemplary objects. In Fig. 7, a sketch of the two objects is presented. The first object is a 3.5×3.5 mm ceramic square post. The second object is a composite object, where one half is a half-circle glued to the hypotenuse of a right-angled triangle. The object is made from two dielectric materials. The triangle-shaped part is 3D printed from a technical polylactic acid (tough PLA) and the half circle is made of wood. The objects are scanned using a circular scan, where the object is rotated to generate a 2-dimensional image of the target similar to our previous work [15]. Using the measurement setup described in section II-B, 360° circular scans of the two objects for both polarizations are performed. Employing the presented imaging approach, the reconstructed images of the ceramic object and the composite object using the measurements with the s polarized terahertz electric field are shown in Fig. 8. Comparing the two images with the real 2D shape of the test objects, we can conclude that correct reconstruction of the two objects is achieved. However, there are significant differences considering the dynamic range of the two images. Here, we define the dynamic range of the reconstructed image as the difference between the noise floor (shown in green) and the reconstructed contour of the object. The first image exhibits a dynamic range of approximately 25 dB. The image of the composite object has approx. 12 dB dynamic range. This is due to the permittivity of the dielectric materials from which the objects are made. As wood and tough PLA have lower permittivity than ceramic, the detected reflection from the composite object exhibits lower amplitude and thus the dynamic range of the reconstructed image is lower than the one of the ceramic object.

So far only the image of the object is reconstructed. However, for the material estimation of the object, further information is needed, such as the precise contour of the object the relative position of the object's contour to the emitter-detector pair, and information about the features of the object such as edges and corners. For this purpose, further post-processing algorithms are implemented. In the next step the contour of the object is extracted from the migrated terahertz image.

B. CONTOUR EXTRACTION FOR KIRCHHOFF MIGRATED IMAGES

In the next step, the contour of the object is extracted for further material parameter estimation. In the following subsection, a basic contour extraction algorithm for Kirchhoff Migration imaging is employed. The algorithm is an active contour model called snake. The snake approach was first proposed by Kass in 1987 [35]. Since then, the active contour methods have become attractive for image processing applications. In [35], Kass defines the snake as a parametric curve $\mathbf{c}(s) = [x(s), y(s)]$, $s \in [0, 1]$ within an image that deforms depending on internal and external forces to converge to desired features of the contour of an object. The internal force is based on the contour smoothness itself (defined as curves or surfaces). The external force is based on the image data and is typically defined such that the contour changes its shape into the shape of the imaged object. The approach is based on the minimization of the energy function [35]

$$E(\mathbf{c}(s)) = \int_0^1 \frac{1}{2}\left(\alpha\left|\mathbf{c}'(s)\right|^2 + \beta\left|\mathbf{c}''(s)\right|^2\right) + E_{\text{ext}}(\mathbf{c}(s))\mathrm{d}s, \quad (9)$$

where α and β are parameters controlling the tension and rigidity of the snake. The internal energy of the snake is determined by the geometric features of the curve represented by the first two terms within the integral in (9), while the external energy $E_{\text{ext}}(\mathbf{c}(s))$ depends on the image data.

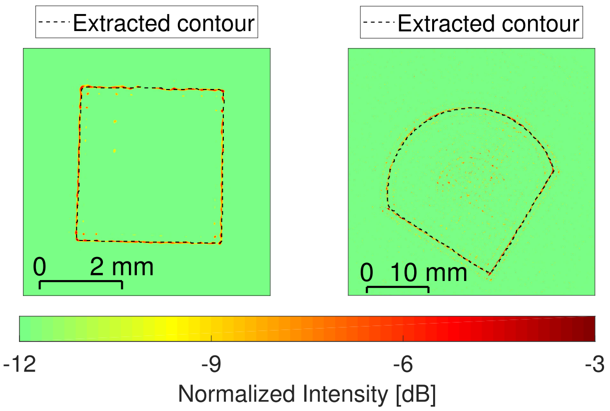

FIGURE 9. Generated image of the two test objects and the extracted contours (black) using the snake algorithm.

Here, we employ the component normalized generalized gradient vector flow (CN-GGVF) [36] as the external force for the snake. The snake is used for the extraction of the contour of the Kirchhoff migrated images of the two samples from Fig. 8. As shown in Fig. 9, the employed approach is capable to extract correct contours from the migrated THz images. However, some fluctuations in the extracted contours are present due to noise and image artifacts. These fluctuations must be separated from important features like corners and edges of the object, which cause diffraction. Hence, the next part of the proposed approach deals with the detection of the features of the extracted contour such as corners and edges.

C. CORNER AND EDGE DETECTION BASED ON CURVATURE SCALE SPACE

Corners of the extracted curvature are important features for the evaluation of the material parameters since diffraction effects have a significant impact on the estimated value. Hence, the detection of corners and edges of the object contour is required. The curvature scale space (CSS) detection has been proposed in [37] as suitable and reliable technique for the detection of corners.

The CSS technique is suitable for recovering invariant geometric features of a planar curve at multiple scales. At first, the parameterized curvature $\mathbf{c}(s)$ from the previous section is convoluted with a Gaussian function $g(s, \sigma)$ where σ is the standard deviation of the Gaussian function. By increasing σ, the contour gets smoother, but the information of the features such as edges or corners may be lost. Distortion that are smaller than the imaging resolution are filtered, while features of the object are maintained. By this convolution, local distortions of the curvature extraction are eliminated. The Gaussian convoluted curvature is

$$\mathbf{c}_g(s) = [x(s) * g(s, \sigma), y(s) * g(s, \sigma)] = [x(s, \sigma), y(s, \sigma)]. \tag{10}$$

The results for $\mathbf{c}_g(s)$ using the contour of the ceramic square for four different values of σ are shown in Fig. 10.a)-d), where σ is 20 μm, 30 μm, 100 μm, and 200 μm, respectively. For $\sigma = 200\,\mu$m, the contour of the four flat surfaces is smooth, but the edges become curved and the angle information about the edges is lost. For $\sigma < 200\,\mu$m, a smoother contour of the test object is achieved, while the edges remain mostly unchanged.

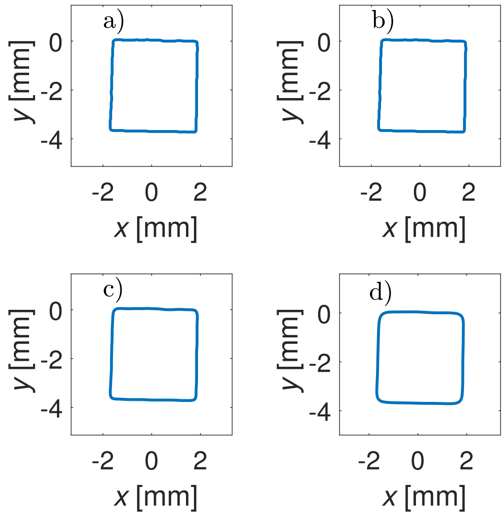

FIGURE 10. Filtered contour of the squared ceramic post test object using a) $\sigma < 20\,\mu$m, b) $\sigma < 30\,\mu$m, c) $\sigma < 100\,\mu$m, and d) $\sigma < 200\,\mu$m.

To find the corners from $\mathbf{c}_g(s)$ of the input curve, the curvature of the contour must be computed. Using the CSS technique, the curvature is calculated as

$$\kappa(s, \sigma) = \frac{x'(s, \sigma)y''(s, \sigma) - x''(s, \sigma)y'(s, \sigma)}{\left(x'(s, \sigma)^2 + y'(s, \sigma)^2\right)^{3/2}} \tag{11}$$

where $x'(s, \sigma)$ and $y'(s, \sigma)$ are the first derivatives, and $x''(s, \sigma)$ and $y''(s, \sigma)$ are the second derivatives considering the x and y direction of the extracted contour.

Using the filtered contour from Fig. 10, the values for $\kappa(s, \sigma)$ are calculated according to (11). The normalized results are presented in Fig. 11. Here, the curvature of the contour is shown as a function of the azimuth angle of the contour in polar coordinates. The peaks in $\kappa(s, \sigma)$ represent discontinuities of the contour such as edges and the constant values of $\kappa(s, \sigma)$ represent the flat surfaces of the object. As the object is square-shaped, four edges i.e. four peaks are detected for $\varphi = 35°$, $\varphi = 125°$, $\varphi = 215°$ and $\varphi = 305°$. However, when the contour is filtered with $\sigma < 100\,\mu$m (blue for $\sigma = 20\,\mu$m and red for $\sigma = 30\,\mu$m) further strong peaks in $\kappa(s, \sigma)$ are detected. This leads to false detection of edges that will result in erroneous calculation of the refractive index. For $\sigma = 100\,\mu$m (orange) and $\sigma = 200\,\mu$m (red) the four strong peaks are correctly detected and the incorrect peaks are attenuated. However, for $\sigma = 200\,\mu$m the information about the edges are partly lost. Hence, we chose $\sigma = 100\,\mu$m for the evaluation of the contour of the test object.

Next, we considered the second test object, which is composed of a triangle and a half circle. In Fig. 12, the CSS of the composite object is presented. Here, we observe three sharp peaks for the three edges of the triangle part of the object, where the rest is approximately constant and only minor changes are observed. As the CSS of a circle is constant,

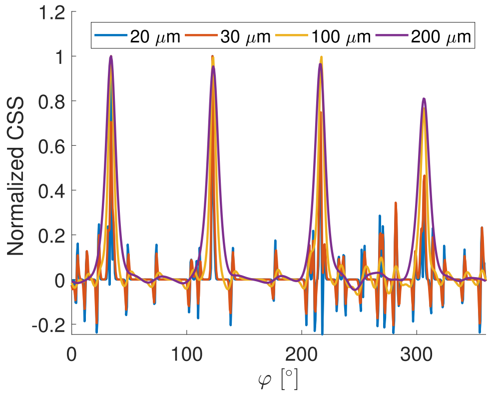

FIGURE 11. Calculated CSS of the filtered contour of the squared ceramic post test object for the four different values of sigma. The peaks demonstrate a sharp change in the contour of the object such as edges and corners.

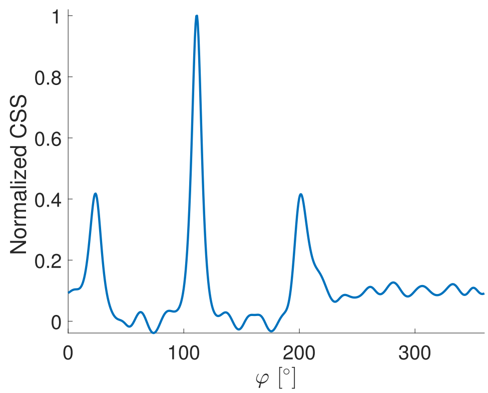

FIGURE 12. Calculated CSS of the filtered contour of the composite test object for $\sigma = 100\,\mu$m. The peaks demonstrate a sharp change in the contour of the object such due to the 3 edges of the object.

the algorithm should result in constant values for the CSS. The present minor deviations of the value originate from to errors in the extraction of the contour for single pixels or roughness of the object's surface.

Once the CSS of the contour is calculated, the algorithms extracts the parts of the objects that contribute to the diffuse reflections, i.e edges. Thus, first the derivative of the $\kappa(s, \sigma)$ and $\kappa'(s, \sigma)$ is calculated in order to detect the peak values of $\kappa(s, \sigma)$. Then, the points of the object's contour are extracted for which $\kappa'(s, \sigma) < \varepsilon$, where $\varepsilon \rightarrow 0$, thus discarding the edges. In Fig. 13, the extracted parts of the objects with dominant specular reflections are highlighted. Using this method, the algorithm correctly detects the four flat surfaces of the square-shaped test object, the two flat surfaces and the half circle surface of the second test object. With this information, the angle of incidence θ_i can be calculated and the material parameters can be estimated. In the following sub-section, the algorithm for the estimation of the material parameter is explained.

D. MATERIAL PARAMETERS ESTIMATION

For the material parameter extraction, we are using the Fresnel equations presented in Section II. As demonstrated, the diffuse reflections from the edges of the test objects lead to

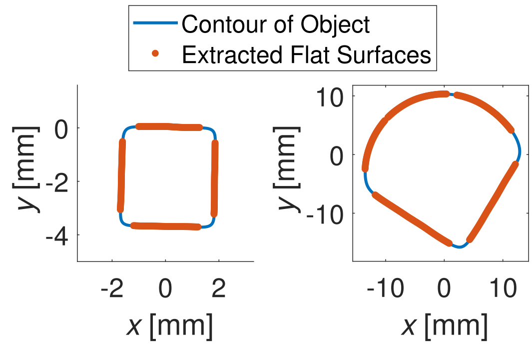

FIGURE 13. Contour (blue) and the extracted surfaces (red) used for the material characterization for the two test objects.

errors in the estimation of the refractive index. Thus, we focus only on the specular reflection. In the previous sub-sections, we derived a method to detect the position of the parts of the test object that contribute to specular reflection. The next step is to extract the specular reflection from the measurement data and to calculate the incidence angle to correctly calculate the refractive index. First, the reflections from the objects are detected for each measurement of both polarization by extracting the amplitudes of the maximum detected electric field according to

$$E_{\mathrm{p},n} = \max\left(|s_\mathrm{p}(t, \mathbf{D}_n, \mathbf{E}_n)|\right) \tag{12}$$

and

$$E_{\mathrm{s},n} = \max\left(|s_\mathrm{s}(t, \mathbf{D}_n, \mathbf{E}_n)|\right), \tag{13}$$

where $\mathbf{D}_n$ and $\mathbf{E}_n$ are the positions of the detector and emitter for the n-th measurement; $s_\mathrm{p}(t, \mathbf{D}_n, \mathbf{E}_n)$ and $s_\mathrm{s}(t, \mathbf{D}_n, \mathbf{E}_n)$ are the detected THz signals with p and s polarizations, respectively. These detected amplitudes are then used for the calculation of the refractive index according to (2) .

Next, the angle of incidence is calculated. For this purpose, the point of reflection from the test object and the relative position of the emitter-detector pair have to be determined. Hence, first the round-trip times of the reflections are extracted from the detected signals as

$$t_{\mathrm{p},n} = \arg\max_t\left(|s_\mathrm{p}(t, \mathbf{D}_n, \mathbf{E}_n)|\right) \tag{14}$$

and

$$t_{\mathrm{s},n} = \arg\max_t\left(|s_\mathrm{s}(t, \mathbf{D}_n, \mathbf{E}_n)|\right). \tag{15}$$

From this, the angle of incidence is calculated. Therefore, the intersection point of the extracted round-trip times with the extracted flat surfaces of the objects contour are calculated. Due to the bistatic antenna configuration (cf. Fig. 3), the intersection point between the extracted round-trip time $t_{\mathrm{p/s},n}$ and the flat surfaces of the object's contour is positioned along an ellipse with focal points $\mathbf{D}_n$ and $\mathbf{E}_n$ and with major and minor axis

$$a_{\mathrm{p/s},n} = \frac{t_{\mathrm{p/s},n} \cdot c}{2}, \tag{16}$$

$$b_{\mathrm{p/s},n} = \sqrt{a_{\mathrm{p/s},n}^2 - e^2}, \tag{17}$$

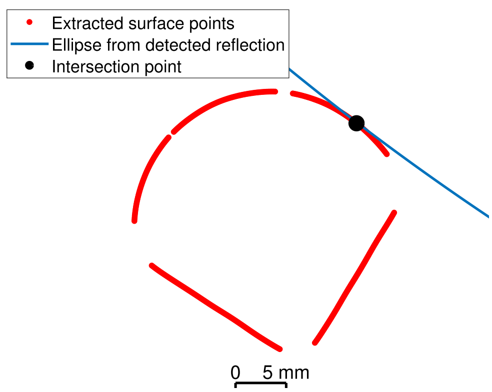

FIGURE 14. Example of derivation of an intersection point. The coordinates of the extracted surface points (red) are intersected with the ellipse calculated from a detected reflection from the test object (blue) resulting in the intersection point shown (black).

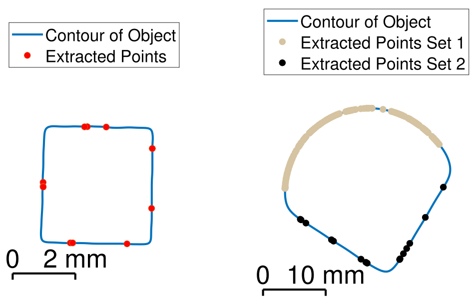

FIGURE 15. Extracted points for the estimation of the material parameters of the two test objects.

where c is the phase velocity and e is half the distance between the emitter $\mathbf{E}_n$ and the detector $\mathbf{D}_n$. The ellipse can then be determined as

$$f_n(x, y) = \frac{x^2}{a^2_{\mathrm{p/s},n}} + \frac{y^2}{b^2_{\mathrm{p/s},n}} - 1 = 0. \tag{18}$$

The intersection point $\mathbf{P}_n$ of the ellipse and the surfaces of the extracted contour is $\mathbf{c}_{\mathrm{fs}}(s) \cap f_n(x, y) == \mathbf{P}_n$. An example for the derivation of an intersection point is shown in Fig. 14. Here, the coordinates of the extracted surface points (red) from Fig. 13 and an ellipse resulting from a detected reflection from the test object are shown. The intersection point (blue) is then derived as the intersection of the two graphs. In Fig. 15, the extracted intersection points for the two objects are shown. Although, the test objects are symmetrical, the extracted intersection points are not. This can be due to the position of the test object on the rotation stage. If the test object is not perfectly centered, the specular reflection will occur at different angles of incidence and positions on the test object. The angle of incidence $\theta_{\mathrm{i},n}$ is then

$$\theta_{\mathrm{i},n} = \frac{1}{2} \arccos\left(\frac{(\mathbf{P}_n - \mathbf{E}_n)(\mathbf{D}_n - \mathbf{P}_n)}{|(\mathbf{P}_n - \mathbf{E}_n)||(\mathbf{D}_n - \mathbf{P}_n|}\right). \tag{19}$$

Now, with the correct angle of incidence $\theta_{\mathrm{i},n}$ and The estimated mean value of the refractive index of the first test object (squared ceramic post) is $n_{\mathrm{r,c}} = 3.02$ with the variance $\sigma^2_{\mathrm{r,c}} = 0.009$. The results show a small deviation from the expected values for ceramic ($n_{\mathrm{r}} \approx 3.1$). In the case of the second test object, we estimated two mean values for the refractive index based on the extracted points from set 1 and set 2 (cf. Fig. 15). For the first set of points of the composite object representing the wooden area of the object, the estimated mean value of the refractive index is $n_{\mathrm{r,w}} = 1.5$ with the variance $\sigma^2_{\mathrm{r,w}} = 0.001$. The estimated refractive index agrees with the values for wood in the literature [38]. For the second set of extracted points, the estimated mean value is $n_{\mathrm{r,PLA}} = 1.73$ with the variance $\sigma^2_{\mathrm{r,PLA}} = 0.006$. This values agree with reference spectroscopic measurements in transmission mode of 3D printed tough PLA, where we measured values for the refractive index of tough PLA of around 1.7.

IV. CONCLUSION

In this paper, we presented a new reference-free material characterization approach for THz TDS systems in reflection mode for objects with unknown shape, orientation, and relative position with respect to the emitter-detector. To overcome this challenge, we employed a multistage procedure consisting of four steps, where in each step information about the object's geometry is extracted. We combined a lensless terahertz imaging approach with conventional contour extraction and edge detection techniques for the complete geometrical description of the test object. The extracted information is then used for the estimation of the refractive index by using p and s polarized terahertz radiation. A state-of-the-art THz TDS system is used in reflection mode for the proof-of-concept of the proposed approach. Two different dielectric objects were used as test objects for the method, namely a 3.5 mm ceramic post and a composite object created from a 3D printed PLA glued to half-circle wooden post. From the ceramic post, the proposed method estimated a value for the refractive index of $n_{\mathrm{r,c}} = 3.02$. This result shows a small deviation compared with the value for the refractive index of the material of 3.1 measured using the well established THz spectroscopy measurement technique presented in [2]. For the second test object, the estimated refractive index for the wooden part is $n_{\mathrm{r,w}} = 1.5$ which is well in the range of literature values for wood [38]. The value for the 3D printed tough PLA part is with $n_{\mathrm{r,PLA}} = 1.73$ in agreement with the measured value of 1.7 from a conventional THz TDS measurement. With the composite test object, we demonstrated the capability of the method to differentiate between two dielectric materials. It is noteworthy that the method enables the retrieval of valid values for the refractive index of relatively small objects although ellipsometry works best for large plane surfaces. Further investigation of the material characterization method will be performed for complex objects before extending the method for 3-dimensional and multilayered objects.

REFERENCES

[1] M. van Exter, C. Fattinger, and D. Grischkowsky, "Terahertz time-domain spectroscopy of water vapor," *Opt. Lett.*, vol. 14, no. 20, p. 1128, Oct. 1989.

[2] P. U. Jepsen, D. G. Cooke, and M. Koch, ''Terahertz spectroscopy and imaging–modern techniques and applications,'' *Laser Photon. Rev.*, vol. 5, no. 1, pp. 124–166, Jan. 2011.

[3] R. B. Kohlhaas, R. J. B. Dietz, S. Breuer, S. Nellen, L. Liebermeister, M. Schell, and B. Globisch, ''Improving the dynamic range of InGaAs-based THz detectors by localized beryllium doping: Up to 70 dB at 3 THz,'' *Opt. Lett.*, vol. 43, no. 21, p. 5423, Nov. 2018.

[4] U. Nandi, J. C. Norman, A. C. Gossard, H. Lu, and S. Preu, ''1550-nm driven ErAs: In(Al)GaAs photoconductor-based terahertz time domain system with 6.5 THz bandwidth,'' *J. Infr., Millim., Terahertz Waves*, vol. 39, no. 4, pp. 340–348, Apr. 2018.

[5] I. Pupeza, R. Wilk, and M. Koch, ''Highly accurate optical material parameter determination with THz time-domain spectroscopy,'' *Opt. Express*, vol. 15, no. 7, p. 4335, 2007.

[6] N. Born, I. Al-Naib, C. Jansen, R. Singh, J. V. Moloney, M. Scheller, and M. Koch, ''Terahertz metamaterials with ultrahigh angular sensitivity,'' *Adv. Opt. Mater.*, vol. 3, no. 5, pp. 642–645, May 2015.

[7] A. M. Adbul-munaim, M. Reuter, O. M. Abdulmunem, J. C. Balzer, M. Koch, and D. G. Watson, ''Using terahertz time-domain spectroscopy to discriminate among water contamination levels in diesel engine oil,'' *Trans. ASABE*, vol. 59, no. 3, pp. 795–801, 2016.

[8] W. Withayachumnankul, B. M. Fischer, H. Lin, and D. Abbott, ''Uncertainty in terahertz time-domain spectroscopy measurement,'' *J. Opt. Soc. Amer. B, Opt. Phys.*, vol. 25, no. 6, p. 1059, Jun. 2008.

[9] L. Thrane, R. H. Jacobsen, P. Uhd Jepsen, and S. R. Keiding, ''THz reflection spectroscopy of liquid water,'' *Chem. Phys. Lett.*, vol. 240, no. 4, pp. 330–333, Jun. 1995.

[10] S. Nashima, O. Morikawa, K. Takata, and M. Hangyo, ''Measurement of optical properties of highly doped silicon by terahertz time domain reflection spectroscopy,'' *Appl. Phys. Lett.*, vol. 79, no. 24, pp. 3923–3925, Dec. 2001.

[11] A. Pashkin, M. Kempa, H. Němec, F. Kadlec, and P. Kužel, ''Phase-sensitive time-domain terahertz reflection spectroscopy,'' *Rev. Sci. Instrum.*, vol. 74, no. 11, pp. 4711–4717, Nov. 2003.

[12] E. M. Vartiainen, Y. Ino, R. Shimano, M. Kuwata-Gonokami, Y. P. Svirko, and K.-E. Peiponen, ''Numerical phase correction method for terahertz time-domain reflection spectroscopy,'' *J. Appl. Phys.*, vol. 96, no. 8, pp. 4171–4175, Oct. 2004.

[13] H.-B. Liu, Y. Chen, G. J. Bastiaans, and X.-C. Zhang, ''Detection and identification of explosive RDX by THz diffuse reflection spectroscopy,'' *Opt. Express*, vol. 14, no. 1, p. 415, 2006.

[14] K. Choi, T. Hong, K. I. Sim, T. Ha, B. C. Park, J. H. Chung, S. G. Cho, and J. H. Kim, ''Reflection terahertz time-domain spectroscopy of RDX and HMX explosives,'' *J. Appl. Phys.*, vol. 115, no. 2, Jan. 2014, Art. no. 023105.

[15] D. Damyanov, I. Willms, J. C. Balzer, B. Friederich, M. Yahyapour, N. Vieweg, A. Deninger, K. Kolpatzeck, X. Liu, A. Czylwik, and T. Schultze, ''High resolution lensless terahertz imaging and ranging,'' *IEEE Access*, vol. 7, pp. 147704–147712, 2019, doi: 10.1109/ACCESS.2019.2934582.

[16] J. Sachs, R. Herrmann, M. Kmec, M. Helbig, and K. Schilling, ''Recent advances and applications of M-Sequence based ultra-wideband sensors,'' in *Proc. IEEE Int. Conf. Ultra-Wideband*, Sep. 2007, p. 50.

[17] R. M. A. Azzam and N. M. Bashara, *Ellipsometry and Polarized Light*. Amsterdam, The Netherlands: North-Holland, 1987.

[18] T. Schultze, R. Salman, and I. Willms, ''Microwave ellipsometry and its application in emergency scenarios,'' in *Proc. Int. Konferenz aber Automatische Brandentdeckung (AUBE)*, Duisburg, Germany, Sep. 2009, pp. 395–400.

[19] B. Friederich, T. Schultze, and I. Willms, ''UWB-radar based surface permittivity estimation in hostile and pathless security scenarios,'' in *Proc. IEEE Int. Conf. Ultra-WideBand (ICUWB)*, Sep. 2014, ., pp. 125–128.

[20] R. Zetik *et al.*, ''Cooperative localization and object recognition in autonomous UWB sensor networks,'' in *Ultra-Wideband Radio Technologies for Communications, Localization and Sensor Applications*. Rijeka, Croatia: InTech, 2013.

[21] R. M. A. Azzam and N. M. Bashara, *Ellipsometry and Polarized Light*. Ann Arbor, MI, USA: Univ. Michigan, 1987.

[22] W. Leschnik and U. Schlemm, ''Dielektrische Untersuchung mineralischer Baustoffe in Abhängigkeit von Feuchte-und Salzgehalt bei 2, 45 GHz,'' DGZfP-Berichtsband BB 69-CD, Technische Univ. Hamburg-Harburg, Hamburg, Germany, Tech. Rep. 14, 1999.

[23] R. G. Kouyoumjian and P. H. Pathak, ''A uniform geometrical theory of diffraction for an edge in a perfectly conducting surface,'' *Proc. IEEE* , vol. 62, no. 11, pp. 1448–1461, Nov. 1974.

[24] W. Burnside and K. Burgener, ''High frequency scattering by a thin lossless dielectric slab,'' *IEEE Trans. Antennas Propag.*, vol. 31, no. 1, pp. 104–110, Jan. 1983.

[25] K. Chamberlin and R. Luebbers, ''An evaluation of longley-rice and GTD propagation models,'' *IEEE Trans. Antennas Propag.*, vol. 30, no. 6, pp. 1093–1098, Nov. 1982.

[26] R. Luebbers, ''Finite conductivity uniform GTD versus knife edge diffraction in prediction of propagation path loss,'' *IEEE Trans. Antennas Propag.*, vol. 32, no. 1, pp. 70–76, Jan. 1984.

[27] E.-M. Stübling, A. Rehn, T. Siebrecht, Y. Bauckhage, L. Öhrström, P. Eppenberger, J. C. Balzer, F. Rühli, and M. Koch, ''Application of a robotic THz imaging system for sub-surface analysis of ancient human remains,'' *Sci. Rep.*, vol. 9, no. 1, Mar. 2019, Art. no. 3390.

[28] Z. Song, S. Yan, Z. Zang, Y. Fu, D. Wei, H.-L. Cui, and P. Lai, ''Temporal and spatial variability of water status in plant leaves by terahertz imaging,'' *IEEE Trans. THz Sci. Technol.*, vol. 8, no. 5, pp. 520–527, Sep. 2018.

[29] E. Stübling, Y. Bauckhage, E. Jelli, B. Fischer, B. Globisch, M. Schell, A. Heinrich, J. C. Balzer, and M. Koch, ''A THz tomography system for arbitrarily shaped samples,'' *J. Infr., Millim., Terahertz Waves*, vol. 38, no. 10, pp. 1179–1182, Oct. 2017.

[30] T. D. Dorney, J. L. Johnson, J. Van Rudd, R. G. Baraniuk, W. W. Symes, and D. M. Mittleman, ''Terahertz reflection imaging using kirchhoff migration,'' *Opt. Lett.*, vol. 26, no. 19, p. 1513, Oct. 2001, doi: 10.1364/ol.26.001513.

[31] A. Bandyopadhyay, A. Stepanov, B. Schulkin, M. Federici, A. Sengupta, D. Gary, J. Federici, R. Barat, Z. Michalopoulou, and D. Zimdars, ''Terahertz interferometric and synthetic aperture imaging,'' *J. Opt. Soc. Amer. A, Opt. Image Sci.*, vol. 23, no. 5, pp. 1168–1178, 2006.

[32] W. A. Schneider, ''Developments in seismic data processing and analysis (1968–1970),'' *Geophysics*, vol. 36, no. 6, pp. 1043–1073, Dec. 1971.

[33] X. Zhuge, A. G. Yarovoy, T. Savelyev, and L. Ligthart, ''Modified kirchhoff migration for UWB MIMO array-based radar imaging,'' *IEEE Trans. Geosci. Remote Sens.*, vol. 48, no. 6, pp. 2692–2703, Jun. 2010.

[34] T. Sakamoto, T. Sato, P. J. Aubry, and A. G. Yarovoy, ''Ultra-wideband radar imaging using a hybrid of kirchhoff migration and stolt F-K migration with an inverse boundary scattering transform,'' *IEEE Trans. Antennas Propag.*, vol. 63, no. 8, pp. 3502–3512, Aug. 2015.

[35] M. Kass, A. Witkin, and D. Terzopoulos, ''Snakes: Active contour models,'' *Int. J. Comput. Vis.*, vol. 1, no. 4, pp. 321–331, 1988.

[36] Y. Zhao, C. Zhu, L. Qin, H. Bai, and H. Tian, ''Component-normalized generalized gradient vector flow for snakes,'' in *The Era of Interactive Media*. New York, NY, USA: Springer, 2013.

[37] F. Mokhtarian and R. Suomela, ''Robust image corner detection through curvature scale space,'' *IEEE Trans. Pattern Anal. Mach. Intell.*, vol. 20, no. 12, pp. 1376–1381, Dec. 1998, doi: 10.1109/34.735812.

[38] K. Krügener, S. Sommer, E. Stübling, R. Jachim, M. Koch, and W. Viöl, ''THz properties of typical woods important for European forestry,'' *J. Infr., Millim., Terahertz Waves*, vol. 40, no. 7, pp. 770–774, Jul. 2019.

BENEDIKT FRIEDERICH received the M.S. degree in electrical engineering from the University of Duisburg-Essen, Duisburg, Germany, in 2013, where he is currently pursuing the Ph.D. degree.

Since 2013, he has been a Research Assistant with the Chair of Communication Systems, University of Duisburg-Essen. Since 2016, he has been a Fellow with the MARIE Project for mobile material characterization and localization by electromagnetic sensing using mobile THz systems. His research interests include digital signal processing for radar applications in terms of synthetic aperture for fire and security applications and especially joint imaging and material characterization techniques.

DILYAN DAMYANOV received the master's degree in communication engineering from the University of Duisburg-Essen, Germany, in 2014, where he is currently pursuing the Ph.D. degree in electrical engineering.

Since 2014, he has been a Research Assistant with the Chair of Communication Systems, University of Duisburg-Essen. Since 2016, he has been a part of the MARIE project for mobile material characterization and localization by electromagnetic sensing using mobile THz systems. His research interests include broadband radar sensors for fire and security applications, especially radar localization, wavefront detection, and imaging techniques.

JAN C. BALZER was born in Unna, Germany, in 1984. He received the Dipl.-Ing. (FH) degree in telecommunications from the Dortmund University of Applied Science, Germany, in 2008, and the M.Sc. degree in electrical engineering and information technology and the Ph.D. degree in electrical engineering (ultrafast semiconductor lasers) from Ruhr-Universität Bochum, Germany, in 2010 and 2014, respectively.

In 2015, he joined the Group of Prof. Martin Koch, Philipp-Universität Marburg, as a Postdoctoral Research Fellow. Since 2017, he has been an Assistant Professor with the Faculty of Engineering, University of Duisburg-Essen, where he combines his knowledge of ultrafast semiconductor lasers with his expertise in system building of THz spectrometers. His main research interest includes THz technology and its application.

THORSTEN SCHULTZE received the Diploma and Ph.D. degrees in electrical engineering from the University of Duisburg-Essen, in 2003 and 2010, respectively.

He is currently an Academic Senior Councillor (Akademischer Oberrat) with the Chair of Communication Systems, University of Duisburg-Essen. His main research interests include automatic fire detection technologies, broadband microwave, and THz analyses for fire and security applications.

DOI: 10.1109/ACCESS.2020.3029355
URN: urn:nbn:de:hbz:464-20210211-113134-1